Rapid Communications in Mass Spectrometry

WILEY

Rapid Communications in Mass Spectrometry

RESEARCH ARTICLE

Generalization of the CCS-Mass Equation to Account for Variations in Molecular Density in an Iron-Ligand Complex Growing System

Christopher Kune[1] | Johann Far[1] | Sophie Rappe[1] | Jean Haler[1] | Albert Demonceau[2] | Lionel Delaude[2] | Gauthier Eppe[1] | Edwin De Pauw[1]

[1]Mass Spectrometry Laboratory, MolSys Research Unit, University of Liège, Liège, Belgium | [2]Laboratory of Catalysis, MolSys Research Unit, Université de Liège, Institut de Chimie Organique (B6a), Liège, Belgium

Correspondence: Edwin De Pauw (e.depauw@uliege.be)

Received: 8 January 2025 | **Revised:** 28 March 2025 | **Accepted:** 28 March 2025

Funding: This work was supported by Fonds De La Recherche Scientifique FNRS and Université de Liège.

Keywords: Ion Mobility | Inorganic complexes | CCS-Mass Trends | apparent density

ABSTRACT

Rationale: In this work, the CCS-mass trends equation has been revisited to consider apparent changes in the ion density.

Methods: The ion mobility-derived collision cross section (IM-derived CCS) of negatively, single-charged Fe(II) and Fe (III) metal centers coordinated with three or four halide or linear alkyl carboxylate ligands generated by electrospray operating in the negative ionization mode were obtained using a T-wave mobility cell.

Results: The CCS-mass trends were fitted using the equation $CCS = A \times mass^{Pow}$ (where A is an apparent density parameter and *Pow* is a shape parameter). Iron-halide complexes led to *Pow* parameters well below the typical limit of 0.5, which could only be explained by refining the fitting equation using a linear combination of these A and *Pow* parameters. Their physical meaning is described in terms of mass distribution within the volume of the iron-ligand complex ions.

Conclusions: The analysis of the CCS-mass trend of iron-halide and iron-carboxylate complexes allows us to predict the IM-derived CCS and the CCS-mass trends of combinations of iron-halide/carboxylate complexes. The results show no differences in trend between planar trigonal and tetrahedral geometries as described by the valence shell electron pair repulsion (VSEPR) theory.

1 | Introduction

Ion mobility spectrometry (IMS) is a gas-phase separation technique taking advantage of collisions between an inert gas and ions accelerated in an electrical field. The separation is driven by the charge states, (reduced) masses, and the ion shapes. After calibration, a property called the Collision Cross Section (CCS) is obtained [1, 2]. From the ion shape (tridimensional volume), the collision surface obtained can be seen in a first approximation as the projection of a rotationally averaged ion shape (volume). Most of the published CCS values are IM-derived, obtained from experimental mobility (K) and reduced mobility values (K_0). Depending on the ion mobility device, the ions acquire either a constant velocity (Drift Tubes, DT), a mean constant velocity (Travelling Wave Ion Mobility Spectrometry TWIMS), or are trapped and stopped (Trapped Ion Mobility or TIMS). The measurable quantities are either the arrival time distribution in drift tube ion mobility spectrometers (DTIMS) [2–4] and traveling wave ion mobility spectrometers (TWIMS) [2, 5, 6] or the elution voltage in trapped ion mobility spectrometers (TIMS) [7–12].

Christopher Kune, Johann Far, Gauthier Eppe, and Edwin De Pauw are equally contributed to the work.

Under the low-field limit [3, 4], these measurable quantities can be converted into CCS values that are related to the mobility K or K_0 according to the Mason–Schamp equation [4]. The mobility values also depend on the buffer gas properties (i.e., pressure, temperature, and polarizability). CCS values can be directly deduced from the IMS data by applying the Mason–Shamp equation [13] for drift tube instruments (DTIMS), or derived from a calibration procedure for TWIMS and TIMS devices. CCS determinations without IMS calibration were also proposed for TWIMS [14, 15] and TIMS instruments [11]. The ion mobility devices are often hyphenated to mass spectrometry (IM-MS) taking advantage of both m/z (MS) and shape separation (IMS) [6] that can be used as ion descriptors. Increasing the mass at constant charge leads to an empirical correlation between the CCS value and the mass of analytes called the CCS-mass trend or CCS-mass correlation. The fitting of this correlation depends on the rotationally averaged global shape of the ions in the gas phase [16]. For a constant shape, typical CCS-mass correlations depend on the average atomic composition in a specified projected volume (i.e., the CCS). Characteristic trends are specific for families of compounds (peptides, lipids, polymers) [9, 17–21]. These CCS-mass trends can be fitted using a power law fit function (Equation 1).

$$CCS = A \times Mass^{Pow} \quad (1)$$

In this equation, the *A* and *Pow* fit parameters are assumed to be related, respectively, to the ion apparent density (i.e., the mass that fits inside the IM-derived *CCS* instead of a real volume) and the ion global shape (or ion geometry or topology) [21–23]. Haler and co-workers have associated the *Pow* parameter with specific shape evolutions considering the projection area of purely geometric and convex models. A *Pow* parameter of 2/3 (0.667) is expected for isotropically growing systems or any system subjected to free rotation and having no preferential orientation in the IMS cell. Anisotropic growing affects the *Pow* parameter [23, 24]. Such a 0.667 *Pow* value is typical for biomolecules [25] and synthetic polymers [21, 22]. Systems growing with a *Pow* parameter comprised between ≈0.9 and ≈1 correspond to cylindrical shape growing with a constant diameter, while cylinder growing with a constant length but an increasing diameter gives a *Pow* value approaching but still greater than 0.5 [23]. Lastly, a *Pow* parameter of 0.89 ± 0.04 was observed for the CCS-mass trend of artificial molecular switches having an elongated structure [24].

In this work, we report on growing systems with CCS-mass trends significantly deviating from those described earlier. This suggests that other properties contribute to the *Pow* parameter in addition to the shape of the ions, among which, their polarizability, temperature, and charge distributions [26–28]. We focus in this paper on how the collision surface increases upon mass addition taking into account the inhomogeneity of mass distribution within the apparent density and the charge distribution. Variations of the apparent density (considered as the ion mass divided by the ion projected volume) and partial charge distributions (or dipole moments) due to the growing system are two properties investigated as factors influencing the CCS-mass trends. Apparent density variations occur when the shape of the ions or the chemical composition (or atomic percent, at.%) of homologous series is not constant throughout the CCS-mass trend. The variation of the system shape affects the CCS value and thus the apparent volume, resulting in a modification of the apparent density. Since the apparent density could also be dependent on the mass and volume of the atoms (Van der Waals volumes) constituting the system, a modification of the atomic percent will directly influence the apparent density value.

It has already been reported that the IM-derived CCS values depend on the ion-induced dipole interactions between the analyte ion and the buffer gas molecules [29]. These interactions depend on the partial charges distribution of the analyte and the polarizability of the buffer gas [30–32]. This can be driven by the geometry of the ions. It is therefore interesting to check whether the valence shell electron pair repulsion (VSEPR) theory (Gillespie–Nyholm models) is still valid in the absence of solvent.

The CCS-mass trends of complex ions consisting of iron (II) or iron (III) halides (i.e., chloride, bromide, and iodide), which are the most structurally compact anions, and carboxylates, which are the structurally most extended anions (i.e., ethanoate, propionate, butanoate, hexanoate, octanoate, and dodecanoate) were considered as models subjected to free rotation with no preferential orientation in the IMS cell but with inhomogeneous mass distribution and different geometries in terms of VSEPR theory. Additionally, the halide and carboxylate iron complexes investigated would empirically occupy the largest CCS-mass space possible. Generalization of the CCS-mass trend equation (Equation 1) is proposed as a result for metal center ions (e.g., metal containing catalysts and advanced inorganic materials).

2 | Materials and Methods

2.1 | Materials and Sample Preparation

Iron (III) chloride, carboxylic acids, and polyalanine polymers were purchased from Sigma–Aldrich. UPLC MS grade methanol and acetonitrile were purchased from Biosolve. Ultrapure water was freshly prepared from a MilliQ Millipore system. Iron (III) chloride was dissolved in pure methanol to obtain a 0.1 M stock solution. 0.1 M stock solutions of each carboxylic acid were prepared. Acetic acid, propionic acid, butanoic acid, and hexanoic acid were dissolved in water, while octanoic acid and dodecanoic acid were dissolved in acetonitrile. 0.1 M stock solutions of chloride, bromide, and iodide were obtained by dissolving ammonium chloride, ammonium bromide, and sodium iodide in water. The final solution contained 1 mM of iron (III) chloride, 50 μM of chloride, 50 μM of bromide, 10 μM of iodide, and 100 μM of each carboxylic acid in acetonitrile/water (50/50 v/v). This mixture was prepared just before electrospray infusion in the ion mobility mass spectrometer using a 250 μL Hamilton syringe and a syringe pump operating at 4 μL per minute. $Fe^{III}L_4^-$ and $Fe^{II}L_3^-$ complexes generated during the electrospray ionization were monitored by ion mobility mass spectrometry operating in the negative ionization mode.

2.2 | Ion Mobility Mass Spectrometry Experiments

Ion mobility data were acquired using a Synapt G2 HDMS instrument (Waters Corp.) with an electrospray ionization source

(ESI). The source voltage was set to −2.2 kV (negative mode). The sampling cone and extraction cone voltages were set to −30 and −3 V, respectively. The source temperature and desolvation temperature were 150°C and 200°C, respectively. The IMS cell was a traveling wave ion mobility cell (TWIMS cell). The TWIMS buffer gas (or drift gas) was N_2 at 2.58 mbar (90 mL.min^{-1}). The helium cell was filled with helium (5.4×10^{-1} mbar) and the TRAP and TRANSFER cells placed, respectively, before and after the TWIMS cell were filled with argon (2.5×10^{-1} mbar). The pressures were measured using independent capacitance gauges (Oerlikon Q5 Leybold Vacuum, CERAVAC CTR 90) linked to a vacuum controller (Vacom, MVC-UVH multichannel vacuum controller). Velocity and height of the traveling waves were fixed at 2100 m.s^{-1} and 40 V, respectively. Data were processed using MassLynx (v4.1) and peak deconvolutions were achieved using Peakfit (v4.11). Peakfit settings were baseline = linear D2, peak type = spectroscopy and Gauss Amp, peak diffusion references. The TWIMS instrument was calibrated with negatively charged polyalanines [33].

2.3 | Computational Chemistry

The structures of iron-halide complexes (FeX_3^- and FeX_4^-, where X represents chloride, bromide, iodide or a combination of them) were optimized by Hartree–Fock method at the MP2 level of theory with LANL2DZ as basis set. The structures of iron-carboxylate complexes (FeC_3^- and FeC_4^-, where C represents ethanoate, propanoate, butanoate, hexanoate, octonoate, and dodecanoate) were optimized by DFT using Cam-B3LYP as functional. Carbon, hydrogen, and oxygen atoms were described with the 6-31 g(d) basis set while LANL2DZ was used for iron. The theoretical volume values of the systems were determined with a homemade Python software allowing structure volume and surface calculations considering Van der Waals (VdW) atomic radii with a scaling factor. This software used Monte Carlo methods for both volume and surface calculations. A scale factor of 1.9 was chosen to ensure that the calculated system surface was equal to 4 times the experimental CCS values ($S = 4\times CCS$) as suggested in the literature [23, 24, 34–36]. Triplicate of 10.000.000 hits with a spatial resolution of 0.01 Å^3 were simulated for each structure to extract the volume information. This volume is called the VdW volume. The mass density of the system was calculated from the mass/volume ratio.

3 | Results and Discussion

Iron complexes were formed by ionic bonds between a positively charged metal center (Fe^{2+} or Fe^{3+}) and negatively charged halide (compact) or carboxylate (extended) ligands. Because of the use of mass spectrometry, no neutral complex could be investigated. Instead iron (III) with four ligands (FeL_4^-) and iron (II) with three ligands (FeL_3^-) species were detected using an electrospray source operating in the negative ionization mode. A mixture of Fe (III) and ligands produced a large range of different ions depending on the random combination of ligands with Fe (II) and Fe (III), occupying a large range of the CCS-mass space, and having various physicochemical properties that were determined by computational chemistry. Note that a positive ionization mode is also possible, producing different iron-ligand stoichiometries and geometries with z = +1, but with fewer combinations than those obtained from the negative ionization mode. Excepted if isobar ions were coexisting in the mass spectra, each extracted mass of the complexes of interest in the arrival time distribution typically produced single and narrow peaks. We provided some of such arrival time distribution in supporting information (See Figure S3, Figure S4, and Figure S5).

The effects of apparent density, geometry, and charge distribution variations on the CCS-mass trends were investigated separately for each Fe (III) or Fe (II) species identified from its exact mass and isotope pattern. Iron (III) complexes with four ligands (denoted FeL_4^-) and iron (II) complexes with three ligands (denoted FeL_3^-) are the main focus of this work. Density functional density (DFT) computations showed that these ions displayed, respectively, a tetrahedral and a trigonal planar geometry in the gas phase. The notations FeX_4^-, FeC_4^-, and $(FeC_nX_{4-n})^-$ ($1 \le n \le 3$) were used to differentiate tetrahedral complexes resulting from the association of Fe^{3+} cations with halide (X) and carboxylate (C) ligands. The same notation was used for trigonal planar complexes derived from the Fe^{2+} cation (i.e., FeX_3, FeC_3^-, and $(FeC_nX_{3-n})^-$ with $1 \le n \le 2$). The arrival time distributions (ATD) of the tetrahedral complexes were first investigated in terms of CCS-mass trends. Because of the inhomogeneous increment of mass due to the halide or organic ligands (non-constant of the atomic percent values), the apparent densities were assumed to be non-constant between the congeners, contrary to what is observed with polymers, for instance. In terms of mass-to-volume ratios, the halides are denser than the carboxylates. For the geometry influence of CCS-mass trends, the ATD of $Fe^{III}L_4^-$ (tetrahedral geometry) and $Fe^{II}L_3^-$ complexes (trigonal planar geometry) were compared. Additionally, the partial charge distribution effect computed by DFT of heteroleptic complexes on the CCS values and CCS-mass trends in nitrogen polarizable gas was examined.

1. Apparent Density Variation With the System Growing Effect on CCS-Mass Trends

The CCS-mass trends of FeX_4^- and FeC_4^- complexes are plotted in Figure 1A with blue and red lines, respectively. This Figure shows that the CCS-mass correlations of these singly charged complexes are considerably impacted by the mass of the ligands and the volume occupied. The FeC_4^- complexes always led to higher CCS values than the FeX_4^- species of similar mass.

The observation of a higher apparent density is the result of a higher mass contained in the same projected volume measured as IM-derived CCS. The higher the apparent densities, the closer the trend moves to the x-axis. The apparent densities determined experimentally for each complex were related to the density of the ligands (2.978 and 39.918 for FeC_4^- and FeX_4^-), respectively (see Figure 1A). As expected, the apparent density was higher for halide than for carboxylate ligands. The *Pow* parameters of these two CCS-mass trends are also substantially different although they share the same tetrahedral geometry. The *Pow* parameter of FeC_4^- (0.71) is close to the expected value of 2/3, while this fit parameter is equal to 0.19 for FeX_4^-. Note that the CCS-mass trend for a carboxylate ligand coordinated to a Fe (III)Cl_3 core (i.e., $FeCl_3C^-$) was previously determined to fit with

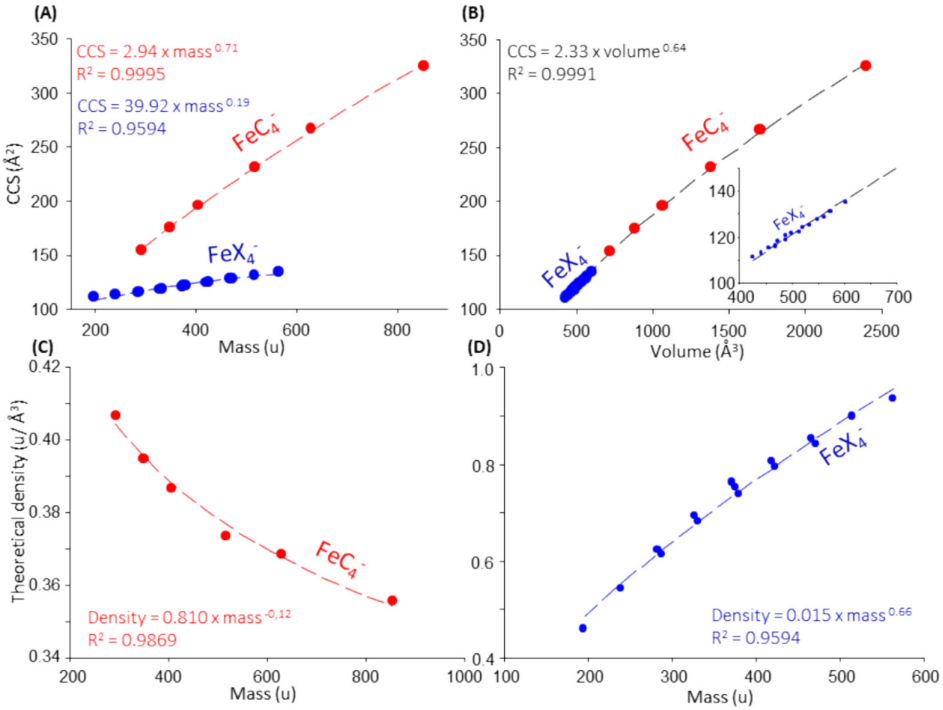

FIGURE 1 | (A) CCS of FeX_4^- and FeC_4^- ions as a function of mass. (B) CCS of FeX_4^- and FeC_4^- ions as a function of the volume considering Van der Waals (VdW) atomic radii. (C) and (D) Theoretical apparent density trends as a function of the $FeC_4^-$and FeX_4^- ion masses, computed from the structures optimized by DFT and our Python script (see Material and Methods for details) considering VdW atomic radii. FeX_4^- (C) and FeC_4^- (D) are represented with blue and red circles, respectively. The fit equations in (A) is expressed as CCS = A × mass ^{pow}, where CCS is the collision cross section, *A* is the apparent density factor, *mass* is the mass of ion in mass unit, and *Pow* is the fit power factor. In (B) the fit equation is CCS = A × volume ^{Pow} were *volume* is the computed volume for the VdW radii. In (C) and (D) fit equation of Density = A × mass ^{pow} where *density* stands for the computed density as mass unit to computed volume ratio.

a *Pow* factor of 0.91 [23] meaning that, as expected, it can be seen as a cylinder growing in length at constant diameter. Here, the rotationally averaged IM-derived CCS of the tetrahedral Fe (III) complexes with carboxylates ligands are seen as near spherical. The *Pow* parameter value of tetrahedral FeX_4^- is quite different from the expected and intuitive value of 2/3. It is important to note that the CCS-mass trends of the calibrating substances involved in IMS calibration (negatively charged polyalanine ions) drastically differs from the FeX_4^- ions (see Figure S1 of the Supporting Information), which could lead to inaccurate CCS determination as suggested by Haler and co-workers [22]. Theoretical *Pow* parameter values of 0.18, 0.17, and 0.16 were computed for ^{PA}CCS-mass, ^{EHSS}CCS-mass and CCS-mass trends (see Figures S1 and S2 of the Supporting Information) in good agreement with the 0.19 experimental value. A systematic bias due to the calibration procedure that would affect the experimental IM-derived CCS should also influence the apparent density fit parameter *A*, but the trends —at least the apparent shape *Pow* fit parameter— were not affected by the calibration procedure.

Figure 1B shows the evolution of the FeC_4^- and FeX_4^- CCS values as a function of their theoretical volumes (calculated from the theoretical structures considering Van der Waals atomic radii). The CCS-volume trends of FeX_4^- and FeC_4^- complexes are defined by the same power fit equation (i.e., the same proportional and power factors) having a power factor close to 2/3 (here 0.64). The rotationally averaged volumes of FeX_4^- and FeC_4^- ions are both converging towards a near-spherical shape.

The CCS-volume correlation of tetrahedral complexes can be expressed with Equation 2. In this equation, the *Volume* factor relies on a volume computed with Van der Waals radii and should therefore not be confused with the apparent volume and the IM-derived *CCS* measured by the IMS device.

$$CCS = Cst \times Volume^{2/3} \tag{2}$$

Equation 2 can be transformed into Equations 3 and 4 since the system volume can be considered as the ratio between its mass and its density (called the *system density* in this work to avoid confusion with the apparent *density*). The *system density* corresponds to the *mass* divided by the real VdW system volume, while the apparent *density* corresponds to the *mass* divided by equivalent IM-derived *CCS* projected volume measured by the IMS. One can consider that the system density and the apparent density are proportional to a particular shape or geometry (see Equation 3). As highlighted in Equation 4, the *A* parameter of CCS-mass trend is thus dependent on the *system density* value, or the apparent *density*, as already reported in the literature [21, 23–25].

$$CCS = Cst \times \left(\frac{mass}{density}\right)^{2/3} \tag{3}$$

$$CCS = \frac{Cst}{systemdensity^{2/3}} \times mass^{2/3} = A \times mass^{2/3} \tag{4}$$

If Equation 4 is valid, all the CCS-mass trends of tetrahedral FeX_4^- and FeC_4^- complexes should have an experimental $CCS = mass^{Pow}$ fit parameter equal to 2/3, since this parameter should not be influenced by the apparent *density* value. Yet, Equation 4 failed to describe the CCS-mass trends of the complex ions under investigation. The initial assumption of this equation is that the ions are growing with constant system density as intuitively suggested by the other fit $CCS = A \times volume^{Pow}$ (with $Pow = 2/3$) in Figure 1B. In Figure 1C and Figure 1D, we show that the theoretical density (calculated as the mass divided by the VdW volume computed from optimized structures) of FeX_4^- and FeC_4^- species varies with their mass. This density evolution within the trends is due to changes in the atomic composition. For example, the replacement of a chloride by a bromide or an iodide (FeX_4^- trend), as well as the replacement of an ethanoate by a hexanoate (FeC_4^- trend), decreases the relative iron mass proportion and increases the ligand mass proportion in the complexes.

To explain why the *Pow* parameter of the CCS-mass trend of FeC_4^- ions (0.71) is closer to the expected 2/3 value for spherical system growing with constant density value than the trend for FeX_4^- species (0.19), we had to revise our hypotheses. The ion density of the investigated complexes was expressed as a power function of the *mass* and two parameters, viz., α, and β (Equation 5). These parameters were fitted from the trends obtained by computational chemistry (cf. Figure 1C and Figure 1D) and are not experimentally derived values.

$$Density = \alpha \times mass^{\beta} \tag{5}$$

Interestingly, the system density values of the FeC_4^- ions were less affected by the mass variation than those of the FeX_4^- ions (see Figure 1C and Figure 1D). This is because the $C_nH_{2n+1}CO_2^-$ carboxylate anions need to occupy a larger volume to weight as much as the Cl^-, Br^-, and I^- halides. In Equation 6, the *CCS* is now expressed as a function of the *mass* considering the α and β fit parameters and the term *Cst* is a constant.

$$CCS = Cst \times \left(\frac{mass}{\alpha \times mass^{\beta}} \right)^{2/3} \tag{6}$$

The development of Equation 6 leads to Equation 7. In this new CCS-mass relation, the A parameter of the CCS-mass trend is still correlated to the density of the complex ion since it depends on the α parameters of the density-mass correlation ($A = Cst/\alpha^{2/3}$). The *Pow* parameter of CCS-mass trends can now be expressed as a function of the β parameter of the density-mass correlation as expressed in Equation 8.

$$CCS = \frac{Cst}{\alpha^{2/3}} \times mass^{2/3 \times (1-\beta)} = A \times mass^{2/3 \times (1-\beta)} \tag{7}$$

$$Pow = \frac{2}{3} \times (1 - \beta) \tag{8}$$

The *Pow* parameters calculated for FeX_4^- and FeC_4^- ions from the β values provided in Figure 1C (−0.12) and Figure 1D (0.66) with Equation 8 are, respectively, 0.22 and 0.74. These theoretical values are in good agreement with the experimental *Pow* parameters (0.19 and 0.71, see Figure 1A). The physical meaning of Equation 8 is that the A parameter of CCS-mass trend is related to the apparent density of the system, while the *Pow* parameter depends, *inter alia*, on the apparent density variation due to the complex size growing and mass distribution. Equation 7 tends to Equation 4 if the apparent density remains constant upon mass variation, i.e., if $\beta = 0$ and the density becomes equal to the α parameter. The CCS-mass trends of homopolymers are perfect examples of density-constant evolution, since the addition of monomers does not affect the element percentages in the polymeric systems.

The effect of the density variation on CCS-mass trends is also supported by the ATD of heteroleptic $(FeX_nC_{4-n})^-$ $(1 \le n \le 3)$ complexes having densities intermediate between those of homoleptic FeX_4^- and FeC_4^- species, as shown in Figure 2A. The CCS-mass trends are plotted as a function of the halide ligands (blue lines) and carboxylate ligands (red lines) in Figure 2B. In both cases, the CCS-mass trends alignments for growing systems suggest that the ligand contributions to the CCS values are independent from each other. The CCS values of these tetrahedral complexes can therefore be determined by considering separately the contributions of the halide and carboxylate ligands as illustrated in Equation 9, where $mass_{Fe}$, $mass_X$, and $mass_C$ are, respectively, the mass of iron, halides, and carboxylates in a complex ion.

$$CCS = f(mass_{Fe}) + f(mass_X) + f(mass_C) \tag{9}$$

The CCS expression in Equation 9 can be developed into a linear combination of the mass contributions for the metal center and the different ligands. Considering the generalized CCS-mass relation (Equation 7) for each ligand type (i.e., halide or carboxylate) reported in Equation 10, A_0, A_1, and A_2 are three fitting parameters that depend on the iron, halide, and carboxylate densities, respectively, while β_X and β_C are the mass-dependence of apparent density parameters for the halide and carboxylate ligands, respectively. All these parameters can be empirically defined.

$$CCS = A_0 + A_1 \times mass_X^{2/3 \times (1-\beta_X)} + A_2 \times mass_C^{2/3 \times (1-\beta_C)} \tag{10}$$

Equation 10 is the expression of a surface with halide and carboxylate masses as variables. The CCS-mass surface for FeX_nC_{4-n} complexes is depicted as a 3D plot in Figure 2C. Gratifyingly, it correctly describes the mobilities of all the tetrahedral complexes investigated in this work. This suggests that the CCS values of FeX_nC_{4-n} heteroleptic complexes can be predicted from the CCS-mass surface equation using the parameters obtained from the CCS-mass trends of their homoleptic FeX_4^- and FeC_4^- cousins. This linear combination can also be applied to the prediction of complexes involving other ligands than halides and

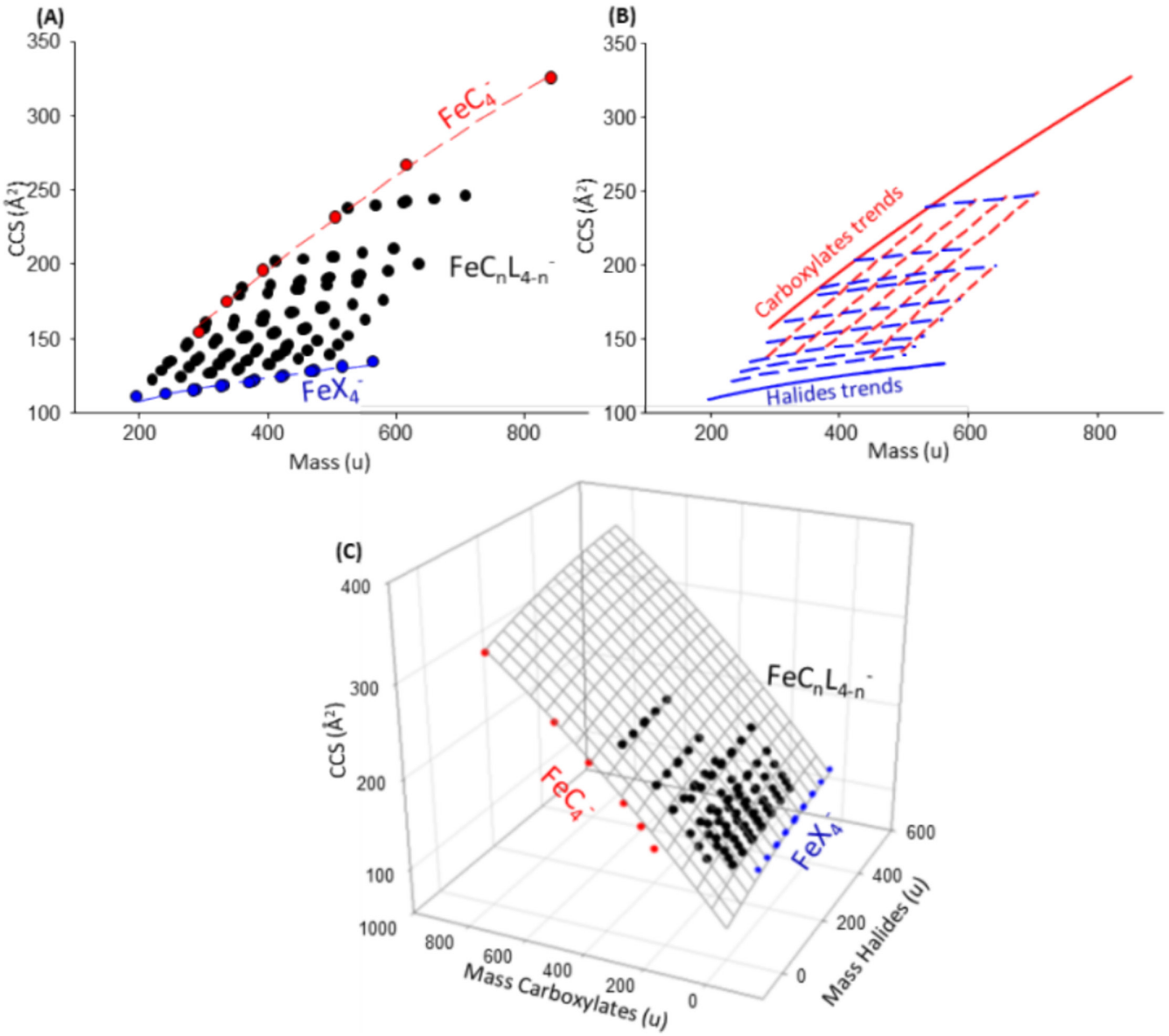

FIGURE 2 | (A) Experimentally IM-derived CCS values as a function of the mass of tetrahedral FeX_4^-, FeC_4^-, and $(FeX_nC_{4-n})^-$ complexes. (B) CCS-mass trends fitted from (A) for $(FeX_nC_{4-n})^-$ complexes highlighting only the halide ligands (blue lines) or the carboxylates ligands (red lines). (C) 3D plot of the IM-derived CCS values (Z-axis) as a function of the carboxylate mass (X-axis) and halide mass (Y-axis). The grid surface represents the prediction obtained by fitting with our power-surface equation (Equation 10).

carboxylates, as soon as the CCS-mass trends of the desired ligands are defined.

2. VSEPR Geometry Effect on the CCS-Mass Trends

The influence of geometry on the CCS-mass correlation was investigated for iron complexes with three ($Fe^{II}L_3^-$) or four ligands ($Fe^{III}L_4^-$). Only homoleptic compounds with halide (FeX_4^- and FeX_3^-) and carboxylate ligands (FeC_4^- and FeC_3^-) were considered to avoid CCS-mass trend differences due to the apparent density heterogeneity of the ligands. Different CCS-mass trends were observed for tetrahedral and trigonal planar geometries (Figure 3A). Interestingly, the *Pow* parameter does not seem to depend on or is only sparsely influenced by the geometry of the ions in the gas phase. *Pow* parameters ranged from 0.70 to 0.71 for iron-carboxylate trigonal and tetrahedral complexes and from 0.18 to 0.19 for their iron-halide counterparts. This is again supported by the similarity of the C parameter of density-mass correlation (Figure 3C and Figure 3D). C parameters were equal to −0.12 for the iron-carboxylate complexes and ranged from 0.65 to 0.66 for the iron-halides derivatives. However, the *A* parameters (pre-power factor of the density-mass correlation in Figure 3C,D) are different (the *A* parameters of FeX_3^- and FeX_4^- are 0.017 and 0.015, respectively, those of FeC_3^- and FeC_4^- are 0.754 and 0.810, respectively). This highlights that the system density of complexes is influenced by the geometry, i.e., complexes with tetrahedral and trigonal planar geometries have different densities for a given mass. Since the *A* parameter of CCS-mass trends relies on the system density, as shown in Equation 4 (for systems that are growing with constant density) and Equation 7 (for systems that are growing with no-constant density), the CCS-mass trends allow the distinction between gas

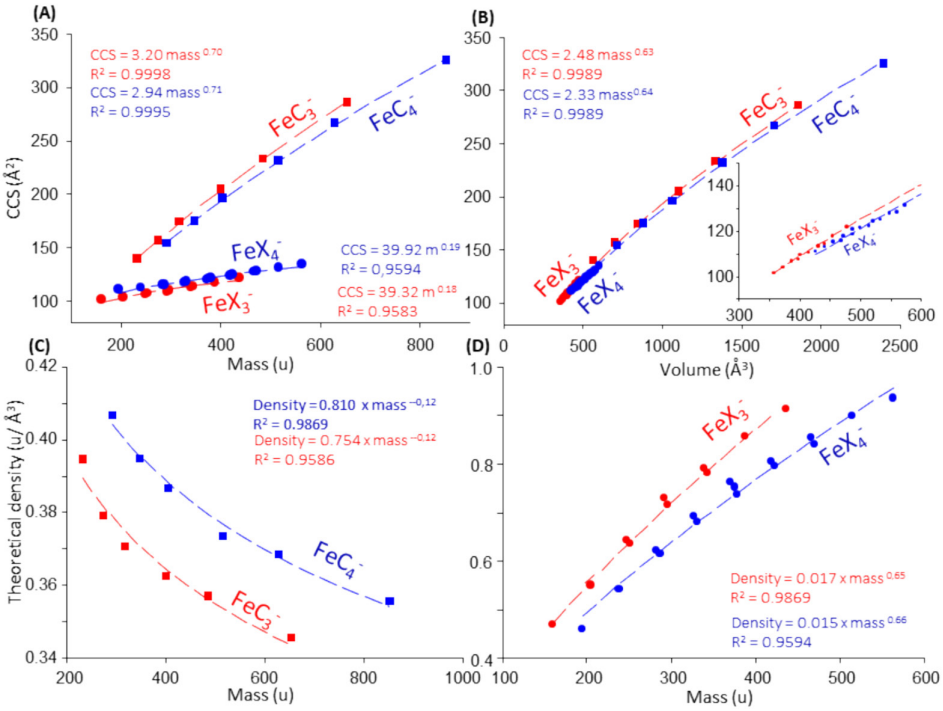

FIGURE 3 | (A) CCS of FeC_3^-, FeC_4^-, FeX_3^-, and FeX_4^- complexes as a function of mass. (B) CCS of FeC_3^-, FeC_4^-, FeX_3^-, and FeX_4^- complexes as a function of the theoretical volume calculated for structures obtained by computational chemistry considering Van der Waals (VdW) atomic radii. (C) Theoretical density (calculated from the theoretical structures obtained by computational chemistry considering VdW atomic radii) as a function of the masses of FeC_3^- and FeC_4^- complexes. (D) Theoretical density (calculated from the theoretical structures obtained by computational chemistry considering VdW atomic radii) as a function of the masses of FeX_3^- and FeX_4^- complexes.

phase trigonal planar and tetrahedral geometries as supported by Figure 3A. Since the *Pow* parameter should be affected by the system shape as reported in the literature [23, 25, 26], one can consider that the trigonal planar and tetrahedral coordination modes are perceived with a similar rotationally averaged apparent near-spherical shape (*Pow* parameter almost equal to 2/3) by the IMS, but with different apparent densities.

It is noteworthy that we performed a similar study using Ni as the metal center because VSEPR predicted a square planar geometry when Ni is coordinating four ligands. The experimental IM-derived CCS-mass trends were very similar to those obtained with iron (data not shown), suggesting either that NiL_4^- complexes do not adopt a square planar geometry, or that the ion mobility resolution (CCS/ΔCCS ≈50) was not sufficient to allow the discrimination between tetrahedral and square planar geometries. As expected, the CCS-mass trends of negative, single-charged Fe(I) ions coordinated by two ligands suggested a linear (cylindrical) geometry (i.e., *Pow* was close to 0.9) when the ligands were carboxylates (data not shown).

3. Effect of Partial Charge Distribution on the CCS-Mass Trends of Heteroleptic Iron Complexes With Halide and Carboxylate Ligands

Heteroleptic complexes of iron with different halide and carboxylates ligands generate different partial charge state distributions that could induce different dragging effects with the buffer gas during ion mobility experiments, as was already demonstrated in a previous study focusing on ruthenium–arene complexes [29]. As shown in Figure 2C, we did not observe significant deviations of the experimental IM-derived CCS of $(FeX_nC_{4-n})^-$ complexes $(1 \leq n \leq 3)$ from the CCS-mass trends that would be explained by the effect of partial charge distribution. Hence, either the partial charge state distribution does not induce preferred rotational averaging of the IM-derived CCS for the iron complexes, or the polarizability volume of nitrogen was still too weak to observe such an effect at a significant level under the limit of ion mobility resolution and CCS accuracy of the spectrometer used in this work.

4 | Conclusions

The effect of inhomogeneous apparent density on CCS-mass trend parameters has been evidenced for iron-halide and iron-carboxylate complexes. This effect can be modeled using a linear combination of a second term in the power equation defining trends that somewhat represent the effect of mass distribution within the ions yielding a rotationally averaged IM-derived CCS. This explains how the ion mobility apparent shape described as the *Pow* parameter in our CCS-mass trends could be as low as 0.18, while *Pow* parameters below 0.5 were not observed for organic compounds, such as synthetic polymers or biopolymers. A unique CCS does not allow shape determination without structure modeling. In the case of trends for families of compounds, the *Pow* value is related to the isotropic or anisotropic growth of the system. We show here that this can however be biased by apparent density inhomogenities (i.e., mass distribution).

The tool that we propose in this work could be applied to other metal complexes, such as homogeneous catalysts and advanced

inorganic materials. We also anticipate that a linear combination should remain valid if a third or fourth class of ligand (e.g., nitrite, nitrate, cyanate, thiocyanate, phosphate, carbonate, and phosphine) is added. Whether this would also apply to heavy metal centers or group of atoms bound to polypeptides, saccharides, or nucleobases for predicting the IM-derived CCS of (bio) molecules or compounds of anthropogenic origin remains to be explored.

Only a small difference in shape was observed between solution geometries, the shape being considered close to spherical shape in both rotationally averaged IM-derived CCS of tetrahedral and trigonal planar complexes. The use of nickel as a metal center, which should adopt a square planar geometry according to the VSEPR theory, is indistinguishable from the iron tetrahedral geometry when comparing the CCS-mass trends of different combinations of Ni with halides or carboxylates. In contrast, the linear complexes $Fe(I)C_2^-$ were unambiguously discriminated as the CCS-mass trends of iron and carboxylate ligands evolved as cylindric shape of constant diameter but growing length.

Last but not least, our data suggest that the partial charge distribution does not significantly affect the CCS-mass trends, at least for the heteroleptic iron complexes with halide and carboxylate ligands studied in this work. The use of an ion mobility mass spectrometer with increased ion mobility resolution and CCS accuracy would be necessary to detect small variations of geometry and induced charge distribution.

Author Contributions

Christopher Kune: conceptualization, investigation, validation, visualization, data curation, software, writing – original draft. **Johann Far:** conceptualization, investigation, validation, visualization, software, writing – original draft. **Sophie Rappe:** investigation, methodology. **Jean Haler:** conceptualization, investigation, methodology, software, writing – original draft. **Albert Demonceau:** methodology. **Lionel Delaude:** methodology, writing – review and editing. **Gauthier Eppe:** funding acquisition, resources. **Edwin De Pauw:** conceptualization, investigation, writing – original draft, writing – review and editing, validation, methodology, supervision, visualization, project administration.

Data Availability Statement

The data that support the findings of this study are available from the corresponding author upon reasonable request.

Peer Review

The peer review history for this article is available at https://www.webofscience.com/api/gateway/wos/peer-review/10.1002/rcm.10042.

References

1. H. E. Revercomb and E. A. Mason, "Theory of Plasma Chromatography/Gaseous Electrophoresis," *Reviews in Analytical Chemistry* 47, no. 7 (1975): 970–983, https://doi.org/10.1021/ac60357a043.

2. R. G. Ewing, "Ion Mobility Spectrometry, 2nd Edition By Gary A. Eiceman (New Mexico State University, Las Cruces, NM) and Zeev Karpas (Nuclear Research Center, Beer-Sheva, Israel). CRC Press (An Imprint of Taylor and Francis Group): Boca Raton, FL. 2005. Xvi + 350 pp. ISBN 0-8493-2247-2," *Journal of the American Chemical Society* 128, no. 16 (2006): 5585–5586, https://doi.org/10.1021/ja0598560.

3. B. C. Hauck, W. F. Siems, C. S. Harden, V. M. McHugh, and H. H. Hill, Jr., "Determination of *E/N* Influence on K_0 Values Within the low Field Region of ion Mobility Spectrometry," *Journal of Physical Chemistry. A* 121, no. 11 (2017): 2274–2281, https://doi.org/10.1021/acs.jpca.6b12331.

4. V. Gabelica, A. A. Shvartsburg, C. Afonso, et al., "Recommendations for Reporting ion Mobility Mass Spectrometry Measurements," *Mass Spectrometry Reviews* 38, no. 3 (2019): 291–320, https://doi.org/10.1002/mas.21585.

5. H. Borsdorf and G. A. Eiceman, "Ion Mobility Spectrometry: Principles and Applications," *Applied Spectroscopy Reviews* 41, no. 4 (2006): 323–375, https://doi.org/10.1080/05704920600663469.

6. A. B. Kanu, P. Dwivedi, M. Tam, L. Matz, and H. H. Hill, "Ion Mobility-Mass Spectrometry," *Journal of Mass Spectrometry* 43, no. 1 (2008): 1–22, https://doi.org/10.1002/jms.1383.

7. F. Fernandez-Lima, D. A. Kaplan, J. Suetering, and M. A. Park, "Gas-Phase Separation Using a Trapped ion Mobility Spectrometer," *International Journal for Ion Mobility Spectrometry* 14 (2011): 2–3, https://doi.org/10.1007/s12127-011-0067-8.

8. K. Michelmann, J. A. Silveira, M. E. Ridgeway, and M. A. Park, "Fundamentals of Trapped Ion Mobility Spectrometry," *Journal of the American Society for Mass Spectrometry* 26, no. 1 (2015): 14–24, https://doi.org/10.1007/s13361-014-0999-4.

9. J. C. May and J. A. McLean, "Ion Mobility-Mass Spectrometry: Time-Dispersive Instrumentation," *Analytical Chemistry* 87, no. 3 (2015): 1422–1436, https://doi.org/10.1021/ac504720m.

10. D. R. Hernandez, J. D. DeBord, M. E. Ridgeway, D. A. Kaplan, M. A. Park, and F. Fernandez-Lima, "Ion Dynamics in a Trapped Ion Mobility Spectrometer," *Analyst* 139, no. 8 (2014): 1913–1921, https://doi.org/10.1039/C3AN02174B.

11. M. E. Ridgeway, M. Lubeck, J. Jordens, M. Mann, and M. A. Park, "Trapped Ion Mobility Spectrometry: A Short Review," *International Journal of Mass Spectrometry* 425 (2018): 22–35, https://doi.org/10.1016/j.ijms.2018.01.006.

12. J. A. Silveira, K. Michelmann, M. E. Ridgeway, and M. A. Park, "Fundamentals of Trapped Ion Mobility Spectrometry Part II: Fluid Dynamics," *Journal of the American Society for Mass Spectrometry* 27, no. 4 (2016): 585–595, https://doi.org/10.1007/s13361-015-1310-z.

13. W. F. Siems, L. A. Viehland, and H. H. Hill, "Improved Momentum-Transfer Theory for Ion Mobility. 1. Derivation of the Fundamental Equation," *Analytical Chemistry* 84, no. 22 (2012): 9782–9791, https://doi.org/10.1021/ac301779s.

14. K. Giles, J. L. Wildgoose, D. J. Langridge, and I. Campuzano, "A Method for Direct Measurement of Ion Mobilities Using a Travelling Wave Ion Guide," *International Journal of Mass Spectrometry* 298, no. 1 (2010): 10–16, https://doi.org/10.1016/j.ijms.2009.10.008.

15. D. N. Mortensen, A. C. Susa, and E. R. Williams, "Collisional Cross-Sections With T-Wave Ion Mobility Spectrometry Without Experimental Calibration," *Journal of the American Society for Mass Spectrometry* 28, no. 7 (2017): 1282–1292, https://doi.org/10.1007/s13361-017-1669-0.

16. R. A. Harris, K. L. Leaptrot, J. C. May, and J. A. McLean, "New Frontiers in Lipidomics Analyses Using Structurally Selective Ion Mobility-Mass Spectrometry," *TrAC Trends in Analytical Chemistry* 116 (2019): 316–323, https://doi.org/10.1016/j.trac.2019.03.031.

17. L. Tao, J. R. McLean, J. A. McLean, and D. H. Russell, "A Collision Cross-Section Database of Singly-Charged Peptide Ions," *Journal of the American Society for Mass Spectrometry* 18, no. 7 (2007): 1232–1238, https://doi.org/10.1016/j.jasms.2007.04.003.

18. L. S. Fenn and J. A. McLean, "Biomolecular Structural Separations by Ion Mobility–Mass Spectrometry," *Analytical and Bioanalytical Chemistry* 391, no. 3 (2008): 905–909, https://doi.org/10.1007/s00216-008-1951-x.

19. J. A. McLean, "The Mass-Mobility Correlation Redux: The Conformational Landscape of Anhydrous Biomolecules," *Journal of the American Society for Mass Spectrometry* 20, no. 10 (2009): 1775–1781, https://doi.org/10.1016/j.jasms.2009.06.016.

20. J. E. Kyle, X. Zhang, K. K. Weitz, et al., "Uncovering Biologically Significant Lipid Isomers With Liquid Chromatography, Ion Mobility Spectrometry and Mass Spectrometry," *Analyst* 141, no. 5 (2016): 1649–1659, https://doi.org/10.1039/C5AN02062J.

21. J. R. N. Haler, D. Morsa, P. Lecomte, C. Jérôme, J. Far, and E. De Pauw, "Predicting Ion Mobility-Mass Spectrometry Trends of Polymers Using the Concept of Apparent Densities," *Methods* 144 (2018): 125–133, https://doi.org/10.1016/j.ymeth.2018.03.010.

22. J. R. N. Haler, C. Kune, P. Massonnet, et al., "Comprehensive Ion Mobility Calibration: Poly (Ethylene Oxide) Polymer Calibrants and General Strategies," *Analytical Chemistry* 89, no. 22 (2017): 12076–12086, https://doi.org/10.1021/acs.analchem.7b02564.

23. J. R. N. Haler, E. Béchet, C. Kune, J. Far, and E. De Pauw, "Geometric Analysis of Shapes in Ion Mobility–Mass Spectrometry," *Journal of the American Society for Mass Spectrometry* 33, no. 2 (2022): 273–283, https://doi.org/10.1021/jasms.1c00266.

24. E. Hanozin, D. Morsa, and E. De Pauw, "Two-Parameter Power Formalism for Structural Screening of Ion Mobility Trends: Applied Study on Artificial Molecular Switches," *Journal of Physical Chemistry. A* 123, no. 37 (2019): 8043–8052, https://doi.org/10.1021/acs.jpca.9b06121.

25. B. T. Ruotolo, J. L. P. Benesch, A. M. Sandercock, S.-J. Hyung, and C. V. Robinson, "Ion Mobility–Mass Spectrometry Analysis of Large Protein Complexes," *Nature Protocols* 3, no. 7 (2008): 1139–1152, https://doi.org/10.1038/nprot.2008.78.

26. C. N. Naylor and B. H. Clowers, "Reevaluating the Role of Polarizability in Ion Mobility Spectrometry," *Journal of the American Society for Mass Spectrometry* 32, no. 3 (2021): 618–627, https://doi.org/10.1021/jasms.0c00338.

27. C. Larriba and C. J. Hogan, "Ion Mobilities in Diatomic Gases: Measurement Versus Prediction With Non-Specular Scattering Models," *Journal of Physical Chemistry. A* 117, no. 19 (2013): 3887–3901, https://doi.org/10.1021/jp312432z.

28. V. D. Gandhi and C. Larriba-Andaluz, "Predicting Ion Mobility as a Function of the Electric Field for Small Ions in Light Gases," *Analytica Chimica Acta* 1184 (2021): 339019, https://doi.org/10.1016/j.aca.2021.339019.

29. I. Czerwinska, J. Far, C. Kune, C. Larriba-Andaluz, L. Delaude, and E. D. Pauw, "Structural Analysis of Ruthenium–Arene Complexes Using Ion Mobility Mass Spectrometry, Collision-Induced Dissociation, and DFT," *Dalton Transactions* 45, no. 15 (2016): 6361–6370, https://doi.org/10.1039/C6DT00080K.

30. L. W. Beegle, I. Kanik, L. Matz, and H. H. Hill, "Effects of Drift-Gas Polarizability on Glycine Peptides in Ion Mobility Spectrometry," *International Journal of Mass Spectrometry* 216, no. 3 (2002): 257–268, https://doi.org/10.1016/S1387-3806(02)00626-7.

31. M. D. Howdle, C. Eckers, A. M.-F. Laures, and C. S. Creaser, "The Effect of Drift Gas on the Separation of Active Pharmaceutical Ingredients and Impurities by Ion Mobility–Mass Spectrometry," *International Journal of Mass Spectrometry* 298, no. 1–3 (2010): 72–77, https://doi.org/10.1016/j.ijms.2009.08.007.

32. M. N. Young and C. Bleiholder, "Molecular Structures and Momentum Transfer Cross Sections: The Influence of the Analyte Charge Distribution," *Journal of the American Society for Mass Spectrometry* 28, no. 4 (2017): 619–627, https://doi.org/10.1007/s13361-017-1605-3.

33. J. G. Forsythe, A. S. Petrov, C. A. Walker, et al., "Collision Cross Section Calibrants for Negative Ion Mode Traveling Wave Ion Mobility-Mass Spectrometry," *Analyst* 140, no. 20 (2015): 6853–6861, https://doi.org/10.1039/C5AN00946D.

34. V. Vouk, "Projected Area of Convex Bodies," *Nature* 162, no. 4113 (1948): 330–331, https://doi.org/10.1038/162330a0.

35. B. R. Jennings, K. Parslow, and R. H. Ottewill, "Particle Size Measurement: The Equivalent Spherical Diameter," *Proceedings of the Royal Society of London. A. Mathematical and Physical Sciences* 419, no. 1856 (1997): 137–149, https://doi.org/10.1098/rspa.1988.0100.

36. G. T. Vickers, "The Projected Areas of Ellipsoids and Cylinders," *Powder Technology* 86, no. 2 (1996): 195–200, https://doi.org/10.1016/0032-5910(95)03049-2.

Supporting Information

Additional supporting information can be found online in the Supporting Information section.